Applied Catalysis B: Environmental 97 (2010) 13–20

Contents lists available at ScienceDirect

Applied Catalysis B: Environmental

journal homepage: www.elsevier.com/locate/apcatb

Modeling of NO_x adsorption–desorption–reduction cycles on a ruthenium loaded Na–Y zeolite

M. Labaki[a,1], M. Issa[b], S. Smeekens[b], S. Heylen[b], C.E.A. Kirschhock[b], K. Villani[b], M. Jeguirim[a], D. Habermacher[a], J.F. Brilhac[a,*], J.A. Martens[b]

[a] Laboratoire Gestion des Risques et Environnement, Université de Haute-Alsace, 25 rue de Chemnitz, 68200 Mulhouse, France
[b] Centrum voor Oppervlaktechemie en Katalyse, Katholieke Universiteit Leuven, Kasteel Arenberg, No. 23, 3001 Heverlee Leuven, Belgium

ARTICLE INFO

Article history:
Received 18 December 2009
Received in revised form 23 February 2010
Accepted 1 March 2010
Available online 6 March 2010

Keywords:
Ru/Na–Y
NO_x storage and reduction
N_2O_3
Kinetic modeling

ABSTRACT

Adsorption of NO from a gas stream containing oxygen and water and desorption and reduction using a rich gas mixture were investigated in the temperature range 230–315 °C on Na–Y zeolite loaded with 3 wt.% ruthenium. The NO_x storage capacity was found little dependent on temperature and water content of the gas. The adsorption–desorption–reduction process was modeled using a one-dimensional fixed-bed model and assuming co-adsorption of NO and NO_2 molecules on Na–Y zeolite, ruthenium catalyzed NO into NO_2 oxidation by molecular oxygen during adsorption and ruthenium catalyzed NO_x reduction by hydrogen during desorption. Kinetic constants were estimated through data fitting. An acceptable agreement between experimental and calculated values was obtained. NO_x adsorption and desorption kinetics on Na–Y zeolite with and without ruthenium were substantially different revealing that ruthenium besides catalyzing NO_x oxidation and reduction had a drastic influence on the NO_x adsorption sites of Na–Y zeolite.

1. Introduction

The combustion of fossil fuel in heating and power generation and in combustion engines of transportation vehicles is the main anthropogenic source of troposphere nitrogen oxides, designated as NO_x. Because of their adverse effect on the environment, reduction of the concentration of NO_x in the atmosphere is a major challenge. Lean burn gasoline engines offer the opportunity to economize fuel and thus to reduce CO_2 emission but their major inconvenience is the formation of nitrogen oxides NO_x. To reduce the NO_x emission in exhaust gas from lean burn engines, essentially two catalytic solutions have been developed: selective catalytic reduction (SCR) and NO_x storage and reduction (NSR). The SCR process consists of reducing NO_x by hydrogen, ammonia, or hydrocarbons. Numerous catalyst materials exhibit SCR activity: perovskite type-oxides like $LaMnO_3$ [1], $LaMn_{0.8}Cu_{0.2}O_3$ [1] and $LaFe_{0.57}Co_{0.38}Pd_{0.05}O_3$ [2], zeolites [3–5], vanadium and tungsten oxide supported on titania, V_2O_5–WO_3/TiO_2 [6], noble metals such as platinum [7], among others.

NSR catalysts were originally presented by Matsumoto [8]. NSR adsorbents provided with catalytic functions are operated in a cyclic process. During lean conditions, NO is oxidized to NO_2 on a precious metal and then trapped on an adsorbent in the form of nitrate. Then, the engine is switched to produce rich exhaust gas for a short period whereupon the trapped NO_x is released and reduced to N_2 thereby regenerating the trap. The NO_x storage function consists of alkaline or alkaline earth metal compounds, dispersed platinum metal and a support, like e.g. in the Pt–Ba/Al_2O_3 catalyst formulation [9]. Driven by the commercial success of the NSR concept, the Pt–Ba/Al_2O_3 catalyst is being intensively investigated [10–14]. Kinetic models [15–17] have been developed for simulating NO_x storage and reduction on Pt–Ba/Al_2O_3 in the presence of exhaust gas components such as CO_2 and H_2O.

The main handicap of the present day NSR formulations is the deactivation caused by sulfur compounds present in fuel and lubricants, sulfates being more stable than nitrates of alkaline earth metals [18–22]. The development of better sulfur-tolerant NSR traps remains an important scientific challenge.

The reactivity of NO_x in zeolites has been known for long time [23]. Among the zeolites Na–Y zeolite presents peculiar NO_x adsorption properties [24–28]. At temperatures exceeding 200 °C, NO and NO_2 are co-adsorbed as N_2O_3 [27,29] and two NO_2 molecules as N_2O_4. Dinitrogen trioxide (N_2O_3) can be formed in dry zeolites upon exposure to nitric oxide [30], to nitric oxide and oxygen [31,32], or to mixtures of nitrogen dioxide and nitric oxide

* Corresponding author. Tel.: +33 3 8932 7656; fax: +33 3 9832 7661.
E-mail address: jean-francois.brilhac@uha.fr (J.F. Brilhac).
[1] Present address: Chemistry Department, Faculty of Sciences II, Lebanese University, Fanar, El-Metn, Lebanon.

0926-3373/$ – see front matter © 2010 Elsevier B.V. All rights reserved.
doi:10.1016/j.apcatb.2010.03.002

Nomenclature

v_{ads}	volumic rate of N_2O_3 formation ($mol_{N_2O_3}\ m^{-3}\ s^{-1}$)
$\rho_{Ru/Na-Y}$	Ru/Na–Y fixed-bed density ($kg\ m^{-3}$) = 640 $kg\ m^{-3}$
$M_{N_2O_3}$	molecular weight of N_2O_3 ($g_{N_2O_3}\ mol^{-1}$) = 76 $g\ mol^{-1}$
k_{ads}	rate constant for N_2O_3 formation (s^{-1})
y	mass fraction of adsorbed N_2O_3 ($g_{N_2O_3}/g_{RU/Na-Y}$)
y_∞	N_2O_3 saturation capacity, taken as the adsorption capacity with 1000 ppm NO in the adsorbing gas ($g_{Ba(NO_3)_2}/g_{RU/Na-Y}$)
X_{NO}	mole fraction of NO in the gas phase
X_{NO_2}	mole fraction of NO_2 in the gas phase
v_{des}	volumic rate of N_2O_3 desorption ($mol_{N_2O_3}\ m^{-3}\ s^{-1}$)
k_{des}	rate constant for N_2O_3 desorption (s^{-1})
X_{H_2O}	mole fraction of H_2O in the phase gas = 0.12 (12%)
v_{oxy}	volumic rate of NO oxidation ($mol_{NO\ or\ NO_2}\ m^{-3}\ s^{-1}$)
k_{oxy}	rate constant for NO oxidation ($mol_{NO\ or\ NO_2}\ kg_{cata}^{-1}\ s^{-1}$)
k_{-oxy}	k_{oxy}/K = rate constant for NO_2 decomposition ($mol_{NO\ or\ NO_2}\ kg_{cata}^{-1}\ s^{-1}$)
α	reaction order with respect to NO
X_{O_2}	oxygen mole fraction in the phase gas
β	reaction order with respect to O_2
v_{desred}	rate of reaction III (red = H_2) ($mol_{N_2O_3}\ m^{-3}\ s^{-1}$)
k_{desred}	kinetic constant of reaction III (red = H_2) (s^{-1})
X_{red}	hydrogen (red = H_2) mole fraction in the phase gas
v_{red3}	rate of reaction IV (v_{redh3}) ($mol_{NO}\ m^{-3}\ s^{-1}$)
k_{red3}	kinetic constant of reaction IV (k_{redh3}) ($mol_{NO}\ kg_{cata}^{-1}\ s^{-1}$)
v_{red4}	rate of reaction V (v_{redh4}) ($mol_{NO_2\ or\ NO}\ m^{-3}\ s^{-1}$)
k_{red4}	kinetic constant of reaction V (k_{redh4}) ($mol_{NO_2\ or\ NO}\ kg_{cata}^{-1}\ s^{-1}$)
dz	L/n = bed length/number of layers into which the bed is divided 1.6×10^{-4} m
s	inlet bed section (m^2) = $2 \times 10^{-4}\ m^2$
F	molar feed rate ($mol\ s^{-1}$) = $6.2 \times 10^{-4}\ mol\ s^{-1}$

[31]. A Rietveld refinement in combination with Fourier analysis of the X-ray diffraction powder pattern of the saturated Na–Y revealed the formation of N_2O_3 [27]. It was shown that N_2O_3 molecules are located at a unique position in the super cage of the zeolite Y. Indeed, the formation of dinitrogen trioxide at 260 °C was monitored by FT-IR spectroscopy [27]. IR absorption bands were assigned to the nitro symmetric stretch, nitro asymmetric stretch, and nitroso stretch, respectively of the asymmetric N_2O_3 conformer. In the same study, Sultana et al. [27] have shown that N_2O_3 formation increases with increasing temperature. It reaches a maximum value at 250 °C. The preferential formation of N_2O_3 is explained by the higher stability of N_2O_3 and the faster association kinetics.

Interestingly, NO_x adsorption on Na–Y zeolite is not affected by the presence of sulfur oxides [27,29–33]. In addition, the advantages of Na–Y zeolite compared to other NO_x adsorbents such as barium oxide on alumina is that the physically adsorbed N_2O_3 molecule can conveniently be evacuated by pressure swing with hydrated inert gas in the absence of reducing agent [33] and that the presence of CO_2 does not affect the NO_x adsorption and desorption in Y type zeolite [26].

In automotive exhaust, NO is the main NO_x compound [34]. For obtaining adsorption of NO_x on Na–Y, oxidation of part of the NO into NO_2 is necessary. Noble metals such as platinum, iridium and ruthenium are active in NO into NO_2 oxidation [35–38] and, in addition, the noble metal can assume a catalytic role in NO_x reduction during a rich phase [13,36,37]. Inspired by the exceptional oxidation activity of ruthenium loaded Na–Y zeolite in NO as well as carbon oxidation [28] ruthenium was selected for this study.

In the present work, the performance of Ru(3%)/Na–Y in view of application in NSR was investigated. The experimental parameters of gas composition and temperature of NO_x adsorption cycles were varied. In a previous publication a mathematical model for NO_x adsorption on Na–Y zeolite has been presented [33]. We extended that adsorption model with ruthenium based NO oxidation and reduction functions and estimated kinetic parameters.

2. Experimental

Zeolite Na–Y (Si/Al ratio 2.71) was obtained from Zeocat. Ruthenium was loaded by the ion-exchange technique using aqueous solution of $RuCl_3$ anhydrous salt (Alfa Aesar, ref: 11,807) at pH 8. The metal loading was 3 wt.% confirmed by ICP analysis of dissolved zeolite sample. The same Ru/Na–Y zeolite material has been evaluated in an earlier study on carbon oxidation [28,38]. Transmission electron microscopy (TEM) pictures of the supported ruthenium particles and powder X-ray diffraction (XRD) patterns have been presented in Ref. [28]. The ruthenium phase is present as nanoparticles dispersed over the Na–Y zeolite.

Experiments were performed on 2.13 g of Ru/Na–Y in a fixed-bed reactor tube mounted in a vertical electrical furnace heated at different temperatures. The adsorbent powder was compressed, crushed and sieved to 250–400 μm and pre-treated for 1 h at 500 °C using a heating rate of 5 °C min^{-1}, under helium flow of 50 L/h (STP) and then cooled to the desired temperature under helium flow. The temperature in the adsorbent bed was monitored with a thermocouple (type K) inserted into the catalyst bed. The gas mixture (NO, O_2 and H_2) was fed from storage cylinders using mass flow controllers. H_2O was added using a thermostatic water evaporator. The total gas flow was 50 L/h which corresponded to a volumetric hourly space velocity (VHSV) of 15,000 h^{-1}. Hydrogen was used as NO_x reducing agent. The typical lean gas consisted of 1050 ppm NO, 5% O_2, 12% H_2O with helium as balance gas. For typical rich conditions, the gas was composed of 1000 ppm NO, 7000 ppm H_2, 12% H_2O with helium as balance gas. It was shown that carbon dioxide and oxygen does not interfere with the NO_x adsorption chemistry in Y type zeolites in the presence of 5% H_2O [26]. Therefore, adsorption–desorption–reduction cycles were conducted without the presence of CO_2 in the gas mixture. NO, NO_2 concentrations at the adsorber outflow were determined using an IR analyzer (Fisher Rosemount Type NGA 2000). The pre-treated adsorbent was first by-passed to control the inlet NO and NO_2 concentration. The lean mixture was then conducted through the Ru/Na–Y bed. After saturation, the adsorbent was again by-passed for a while to allow for a flushing of the lines with the regeneration gas. Subsequently, the regeneration gas was conducted through the saturated bed and the outlet NO and NO_2 concentrations monitored. Cycles including long lean phase and short rich phase, simulating lean burn gasoline engine conditions without sulfur oxides, were repeated 5 times in the temperature range 200–315 °C to verify the reproducibility of the experiments. Adsorption and desorption were always performed at the same temperature. NO_x adsorption capacities were calculated by integration of the NO_x adsorption curves and expressed in $g_{N_2O_3}/g_{catalyst}$. NO conversion into NO_2 in the adsorption phase was calculated after catalyst saturation as follows: $X_{NO_2}/(X_{NO} + X_{NO_2} \times 100)$, where X_{NO} and X_{NO_2} were the outlet mole fractions of NO and NO_2 in the phase gas, respectively.

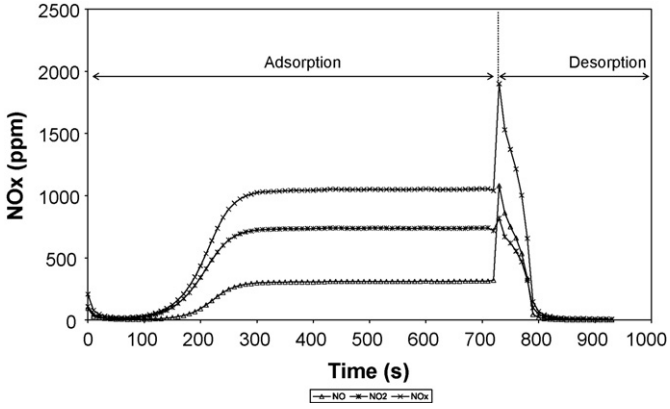

Fig. 1. Outlet NO, NO_2 and NO_x ($NO + NO_2$) concentrations of Ru/Na–Y adsorbent bed at 315 °C against time in the cycle. Simulated lean burn gas mixture: helium with 1050 ppm NO, 5% O_2, 12% H_2O. Rich gas: helium with 1000 ppm NO, 7000 ppm H_2, 12% H_2O.

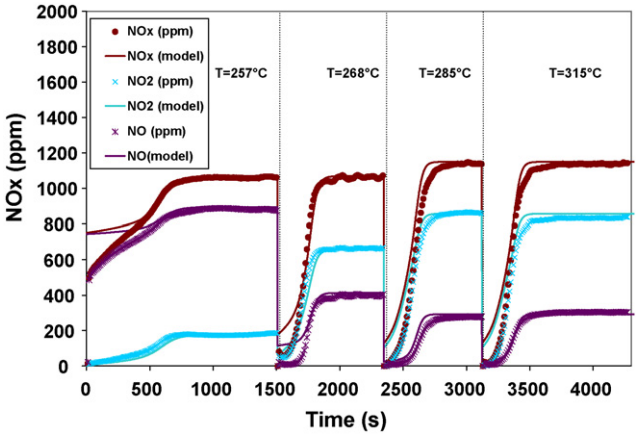

Fig. 2. Experimental outlet NO_x concentration curves (data points) and model (solid lines) of Ru/Na–Y adsorbent at different temperatures. Simulated lean burn gas mixture: helium with 1100 ppm NO, 5% O_2, 12% H_2O. Regeneration using helium with 1000 ppm NO, 7000 ppm H_2, 12% H_2O is not shown.

3. Results and discussion

3.1. Influence of process parameters on NO_x adsorption

3.1.1. Influence of temperature

NO_x adsorption experiments with long lean phases were performed at temperatures between 230 °C and 315 °C in order to evaluate the NO_x storage capacity and the NO oxidation activity. Lean gas mixture was conducted over the Ru/Na–Y adsorbent bed till saturation followed by desorption at the same temperature. An example of a cycle at 315 °C is shown in Fig. 1. In the first 100 s the outlet NO_x concentration was very low because of strong NO_x adsorption. Saturation of the adsorbent, detected by the outlet NO_x concentrations being identical to the inlet concentration of 1050 ppm, occurred around 300 s. The saturated adsorbent acted as a catalyst and oxidized part of the NO into NO_2 with the O_2 from the gas mixture. When after 720 s the inlet gas mixture was changed to rich gas, there was an immediate release of NO_x reaching a peak concentration of ca. 2000 ppm. After 800 s the outlet NO_x concentration dropped to zero. Under rich conditions Ru/Na–Y catalyzed the reduction of the desorbing NO_x as well as the NO_x fed with the rich gas mixture. The adsorption–desorption–reduction cycles were highly reproducible.

During the regeneration step, minor amounts of NH_3 (130 ppm) and N_2O (160 ppm) were detected compared to the maximum of NO_x released. These concentrations represent <5% of the total concentrations and could be neglected. Thus, a minor amount of H_2 was consumed to produce NH_3. These results agree well with those observed by Shelef [39] and Kobylinski and Taylor [40]. They found that the selectivity towards the formation of NH_3 was lower over Rh and Ru than over other noble metal catalysts.

Indeed, the temperature of the catalytic bed (thermocouple was inserted inside the bed of the catalyst) was measured during the switch of H_2 (the regeneration step). The addition of H_2 was accompanied by a small increase of the catalyst temperature (10 °C) which rules out the hypothesis of thermal release of NO_x species. Nova et al. [41] also reported the increase of the catalyst temperature during the switch of H_2. It is of the same order of magnitude (5 °C).

The evolution of the NO_x outlet concentration in adsorption phases of adsorption–desorption–reduction cycles run at different temperatures using similar gas mixtures as in Fig. 1 is shown in Fig. 2. At 257 °C, the outlet NO_x concentration initially was ca. 500 ppm meaning that only about half of the NO_x concentration fed to the adsorber was effectively trapped. With time the outlet NO_x concentration increased and became identical to the inlet concentration indicating saturation of the adsorbent. At 268 °C and higher temperatures, Ru/Na–Y adsorbent removed almost all NO_x from the simulated lean burn gas mixture. Saturation of the adsorbent was noticed by a steep rise of the outlet NO_x concentration. After saturation of the adsorbent, catalytic oxidation of NO over Ru metal continued explaining the presence of NO_2 in the outlet gas. The NO oxidation activity of Ru/Na–Y independent of adsorption phenomena was investigated under such conditions. Table 1 reports the experimental NO_x adsorption capacities and NO into NO_2 conversion on Ru/Na–Y determined in the experiments of Fig. 2.

The NO_x storage capacity remained almost constant in the range of temperatures investigated (Table 1). This NO_x starage capacity of around 2.7 mg N_2O_3/g is similar to the capacity of Na–Y zeolite in NO–NO_2 co-adsorption under similar conditions [27,33]. The NO into NO_2 oxidation conversion increased with temperature from 6% at 230 °C to 70% at 315 °C (Table 1). Després et al. [42] using a 2.5% Pt/SiO_2 catalyst reported that in the temperature range 200–320 °C and in the presence of 5% O_2, NO oxidation into NO_2 was under kinetic control [42], and that at higher temperatures NO into NO_2 conversion was limited by the internal thermodynamic equilibrium, in agreement with observations by other authors [42–44]. The NO into NO_2 conversion typically shows a maximum around 300 °C coinciding with the transition from kinetic to thermodynamic limitation. In the present study, the NO conversion level increased significantly in the temperature interval from 257 °C to 268 °C, while it was only a little higher at 315 °C (Table 1). On Ru/Na–Y

Table 1
NO_x storage capacity ($g_{N_2O_3}$/g) and NO oxidation activity of Ru/Na–Y at different temperatures.

	Temperature (°C)			
	230	257	268	315
N_2O_3 stored[a] ($g_{N_2O_3}$/g)	2.2×10^{-3}	2.4×10^{-3}	2.7×10^{-3}	2.7×10^{-3}
NO conversion into NO_2[b] (%)	6	20	64	70

[a] Determined in adsorption phase of a cycle as $2 \times ([NO_x]_{in} - [NO_x]_{out}) \times VHSV \times t \times M_{N_2O_3}$.
[b] Determined during adsorption phase after saturation with NO_x of the adsorbent.

Table 2
NO_x storage capacity of Ru/Na–Y ($g_{N_2O_3}/g$) at different temperatures for different NO and O_2 concentrations in adsorbing gas containing 12% water.

Temperature (°C)	1050 ppm NO, 2.5%O_2	1070 ppm NO, 5%O_2	1050 ppm NO, 10%O_2	1030 ppm NO, 15%O_2	570 ppm NO, 5%O_2	260 ppm NO, 5%O_2
268	2.5×10^{-3}	2.5×10^{-3}	2.4×10^{-3}	2.3×10^{-3}	2.3×10^{-3}-	1.4×10^{-3}-
285	–	2.9×10^{-3}	–	–	2.5×10^{-3}	1.5×10^{-3}
315	2.5×10^{-3}	2.7×10^{-3}	2.4×10^{-3}	2.3×10	2.2×10^{-3}	1.3×10^{-3}

the transition from kinetic to thermodynamic control over NO oxidation is likely to occur in the temperature window 268–315 °C.

The NO_x desorption process was found not to be affected by the presence of NO in the desorption gas. A similar NO_x storage capacity was obtained with and without NO being present in the gas mixture used for regeneration. NO when present in the gas mixture during regeneration was reduced by hydrogen over the Ru/Na–Y catalyst. The time needed for regeneration detected by the NO_x concentration in the desorbing gas reaching zero was independent of temperature in the range 257–315 °C, while at 230 °C it was slower.

3.2. Influence of NO and O_2 concentration

The NO_x storage capacity of Ru/Na–Y determined using different NO and O_2 concentrations in the adsorbing gas and at different temperatures is reported in Table 2. There was little influence of temperature on the NO_x storage capacity. At a NO inlet concentration to 260 ppm the NO_x storage capacity was significantly lower than at higher NO concentrations. The time needed for saturation of the adsorbent was found to shorten with increasing NO concentration in the feed (Fig. 3).

NO_x adsorption–desorption–reduction cycles at $T = 268$ °C in the presence of different oxygen concentrations ranging from 2.5% to 15% are presented in Fig. 4. The oxygen concentration had little influence on the adsorption traces. The NO_x adsorption capacity (Table 2) was little dependent of the O_2 concentration in the investigated concentration range (2.5–15%). The NO into NO_2 conversion increased with the O_2 content of the gas mixture (Fig. 4).

3.3. Influence of the concentration of reducing agent

NO_x adsorption–desorption–reduction cycles in the presence of different hydrogen contents (0%, 1000 ppm, 3000 ppm and 7000 ppm) in the gas mixture for regeneration were performed at 315 °C. The outlet NO_x concentration traces recorded during different types

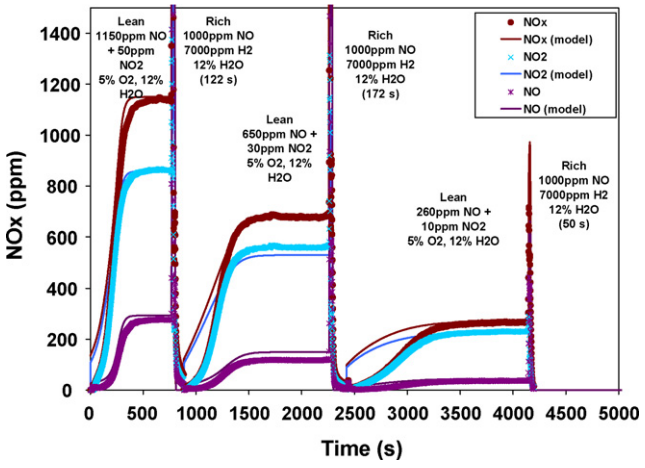

Fig. 3. Experimental outlet NO_x concentrations (data points) and model (solid lines) of Ru/Na–Y adsorbent bed at 285 °C using different NO concentrations in the adsorbing gas mixture. Simulated lean burn gas mixture: helium with 1150 ppm or 680 ppm or 270 ppm NO_x, 5% O_2, 12% H_2O. Rich gas: helium with 1000 ppm NO, 7000 ppm H_2, 12% H_2O.

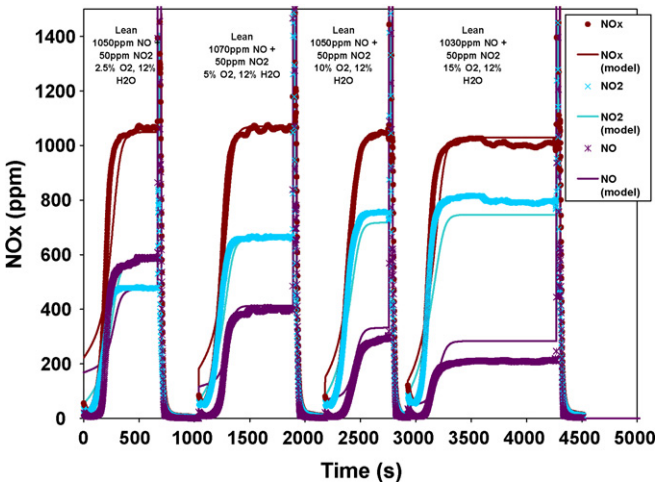

Fig. 4. Experimental NO_x adsorption–desorption–reduction curves (data points) and model (solid lines) at the outlet of Ru/Na–Y sorbent bed at 268 °C using different oxygen concentrations during adsorption. Simulated lean burn gas mixture: helium with 1100 ppm NO_x, 12% H_2O, different inlet mole fractions of O_2: 2.5–15%. Rich gas: helium with 1000 ppm NO, 7000 ppm H_2, 12% H_2O.

of cycles are shown in Fig. 5. In the absence of the reducing agent NO_x desorption was very slow. Hydrogen accelerated NO_x desorption. Using 3000 ppm or 7000 ppm H_2 in the rich phase in cycles at 250 °C and higher, the time needed for NO_x desorption and achieving chemical reduction to reach a zero NO_x concentration level in the outlet was very similar. Thus, a concentration of 3000 ppm H_2 was sufficient to achieve efficient regeneration of the NO_x trap at these temperatures. At 215 °C NO_x desorption and reduction were much slower and when feeding 7000 ppm H_2.

The outlet NO_x concentration profiles during regeneration show that a significant amount of NO_x is not chemically reduced. Probably, at the onset of regeneration ruthenium still is in oxidized form and needs first to be reduced into ruthenium metal which

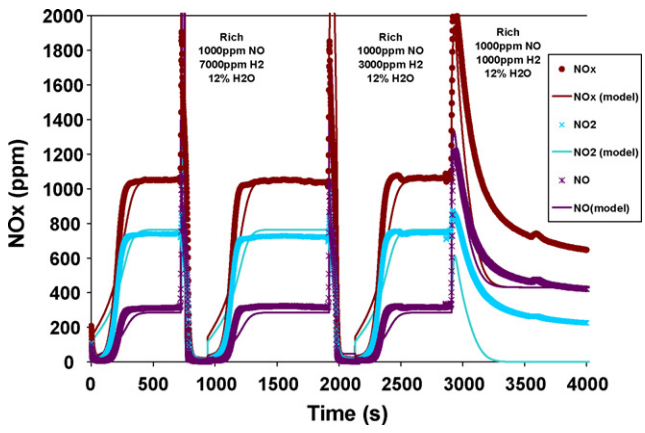

Fig. 5. Experimental NO_x adsorption–desorption–reduction curves (data points) and model (solid lines) at the outlet of Ru/Na–Y sorbent bed at 315 °C using rich gas mixtures with different H_2 content. Simulated lean burn gas mixture: helium with 1050 ppm NO, 5% O_2, 12% H_2O. Rich gas mixture: 7000 ppm, 3000 ppm or 1000 ppm H_2, 1000 ppm NO, 12% H_2O and helium as balance.

is expected to be the active catalyst in NO_x reduction. The time needed for ruthenium reduction may explain the occurrence of a NO_x release peak upon switching gas composition from lean burn to rich.

3.4. Influence of water concentration

NO_x adsorption–desorption–reduction cycles on Ru/Na–Y using gas streams with different water contents (5%, 10%, 12% and 15%) were performed at two different temperatures: 268 °C and 280 °C. No significant differences in the NO_x adsorption and desorption profiles were observed. The NO_x adsorption capacities were similar.

In previous work on the co-adsorption and co-desorption of NO and NO_2 on Na–Y zeolite without ruthenium [33] it was shown that NO_x release was stimulated by water. The higher the water content, the faster the NO_x desorption rate. On Na–Y zeolite, NO and NO_2 co-adsorption as N_2O_3 occurs via the substitution of three water molecules [27]. During desorption, water molecules take over the positions of the adsorbed NO_x in a network of sodium cations and water molecules [27]. In the present study on Ru/Na–Y zeolite, a reducing agent was present in the gas mixture for desorption. Desorption of the NO_x was significantly faster and a positive effect of water on the NO_x desorption rate was no longer observed. The accelerating effect of the reducing agent on the desorption kinetics was much more important than a beneficial influence of the presence of water.

4. Modeling of NO_x adsorption–desorption–reduction cycles

In a previous work [33], a one-dimensional model was proposed for NO and NO_2 co-adsorption and desorption on Na–Y zeolite without ruthenium. The same model could also apply for NO_x adsorption and desorption on Ru/Na–Y assuming that NO and NO_2 co-adsorption takes place on the same sites in Na–Y zeolite, and that ruthenium catalyzes NO oxidation in the lean mixture and NO_x reduction in the rich mixture.

4.1. Adsorption mechanism

4.1.1. Adsorption and desorption of NO/NO_2 on Na–Y

It was assumed that co-adsorption of NO and NO_2 as N_2O_3 on Na–Y takes place by displacing three water molecules. During regeneration it is assumed that water displaces the adsorbed NO and NO_2. The chemical reaction accounting for NO_x adsorption and desorption is as follows:

$$NO + NO_2 + NaY(3H_2O) \underset{k_{des}}{\overset{k_{ads}}{\rightleftarrows}} NaY(N_2O_3) + 3H_2O \quad \text{(I)}$$

4.2. NO oxidation into NO_2

Generally, over 90% of NO_x emitted by engines is present as NO. In this work, NO was the main NO_x compound in the inlet simulated lean burn gas mixture to mimic real gas exhaust. The experimental results revealed that NO was effectively converted into NO_2 in the presence of oxygen on the ruthenium catalyst which enabled the NO–NO_2 co-adsorption (Reaction (I)). This NO oxidation reaction corresponds to:

$$NO + \frac{1}{2}O_2 \underset{k_{-koxy}}{\overset{k_{oxy}}{\rightleftarrows}} NO_2 \quad \text{(II)}$$

The absence of NO oxidation activity on Na–Y zeolite without ruthenium was experimentally verified. Ruthenium catalysts are known for their high activity in oxidation catalysis [45]. Ohtsuka reported ruthenium on sulfated zirconia to be a highly active catalyst for NO oxidation into NO_2 [37]. Taking into consideration that the experiments were run under conditions of kinetic control over NO oxidation at lower temperatures turning into thermodynamic control at higher temperatures, forward and backward reactions were taken into account (Reaction (II)).

The numerical value for the equilibrium constant of Reaction (II) was adopted from Ref. [46]:

$$K = \frac{k_{oxy}}{k_{-oxy}} = 1.0567 \times 10^{-4} \exp\left(\frac{-(-58281)}{RT}\right)$$

4.3. NO/NO_2 desorption in the presence of H_2 under rich conditions

The presence of H_2 in the rich mixture accelerated the NO_x desorption step. Thus, hydrogen needs to be assigned a role during desorption. Hence, for describing the desorption the following reaction equation was used:

$$Ru/Na\text{–}Y(N_2O_3) + 3H_2O + H_2 \overset{k_{desh2}}{\longrightarrow} Ru/Na\text{–}Y(3H_2O) + NO + NO_2 + H_2 \quad \text{(III)}$$

Note that Reaction (III) is a global reaction equation accounting probably for several elementary reaction steps that needed to be lumped because of a lack of insight.

4.3.1. NO and NO_2 reduction by H_2 under rich conditions

NO and NO_2 desorbed during the rich spike were assumed to be reduced by H_2 according to the following reactions:

$$NO + H_2 \overset{k_{redh3}}{\longrightarrow} \frac{1}{2}N_2 + H_2O \quad \text{(IV)}$$

$$NO_2 + H_2 \overset{k_{redh4}}{\longrightarrow} NO + H_2O \quad \text{(V)}$$

It is known that ruthenium may favor the reduction of NO_x into ammonia [47]. For reasons of simplicity it was assumed that all reductions led to N_2. Given the large excess of H_2 with respect to NO_x, formation of N_2 versus NH_3 had little influence on the model.

4.4. Model assumptions

For the building of the model, the following assumptions were made:

(i) quasi steady-state regime,
(ii) temperature gradients are absent,
(iii) no concentration gradients in a plane perpendicular to gas flow direction (z),
(iv) the local rate of N_2O_3 formation (v_{ads}) is proportional to the local concentrations of NO (X_{NO}) and NO_2 (X_{NO_2}) in the gas phase and to the difference between saturation capacity of the adsorbent (y_∞) and the actual locally adsorbed N_2O_3 mass fraction (y)

$$v_{ads} = -\frac{dX_{NO}}{dt} = -\frac{dX_{NO_2}}{dt} = \frac{\rho_{Ru/Na-Y}}{M_{N_2O_3}} k_{ads}(y_\infty - y(z,t))X_{NO}(z,t)X_{NO_2}(z,t)$$

(v) the local rate of N_2O_3 desorption is considered to be proportional to the locally adsorbed mass fraction of N_2O_3 molecules and to the third power of the mole fraction of water in the phase gas:

$$v_{des} = \frac{dX_{NO}}{dt} = \frac{dX_{NO_2}}{dt} = \frac{\rho_{Ru/Na-Y}}{M_{N_2O_3}} k_{des} y(z,t) X_{H_2O}^3$$

Table 3
y_∞ values ($g_{N_2O_3}/g_{cata}$) taken as model input and kinetic constants obtained for Ru/Na–Y at different temperatures. k_{ads}, k_{des}, k_{desh2} and k_{desCO} are given in s^{-1}, k_{oxy}, k_{redh3}, k_{redh4}, k_{redCO_3} and k_{redCO_4} are given in mol s^{-1} kg_{cata}^{-1}.

T (°C)	y_∞	k_{ads}	k_{des}	K	k_{oxy}	k_{-oxy}	k_{desh2}	k_{redh3}	k_{redh4}
257	2.80×10^{-3}	150,000	4.0	58.6	0.022	0.0003	80	400	400
268	2.80×10^{-3}	150,000	4.0	44.8	0.154	0.0034	80	400	400
285	2.80×10^{-3}	150,000	4.0	30.2	0.266	0.0088	80	400	400
315	2.80×10^{-3}	150,000	4.0	15.9	2.437	0.153	80	400	400

(vi) the reaction rate of NO oxidation (NO_2 formation) is:

$$v_{oxy} = -\frac{dX_{NO}}{dt} = \frac{dX_{NO_2}}{dt} = \rho_{Ru/Na-Y} k_{oxy} X_{NO}^{\alpha} X_{O_2}^{\beta} - \frac{k_{oxy}}{K} X_{NO_2}$$

(vii) the rate of Reaction (III) is given by:

$$v_{desred} = \frac{dX_{NO}}{dt} = \frac{dX_{NO_2}}{dt} = \frac{\rho_{Ru/Na-Y}}{M_{N_2O_3}} k_{desred} X_{red} X_{H_2O}^3 y(z,t)$$

(viii) the rates of Reactions (IV) and (V) are given by:

$$v_{red3\,or\,4} = \rho_{Ru/Na-Y} k_{red3\,or\,4} X_{NO\,or\,NO_2} X_{red}$$

4.5. Equations

Taking Reactions (I)–(V) into account the mass balances in an elementary layer of the bed ($dV = s\,dz$) can be expressed. The calculation of $y(z, t)$ depends on time and on z:

$$\left.\frac{dX_{NO}}{dz}\right|_t = \frac{s\rho_{Ru/Na-Y}}{FM_{N_2O_3}} \begin{bmatrix} -k_{ads}(y_\infty - y(z,t))X_{NO}(z,t)X_{NO_2}(z,t) + k_{des}y(z,t)X_{H_2O}^3 \\ +k_{desred}X_{red}(z,t)X_{H_2O}^3 y(z,t) - k_{oxy}X_{NO}^{\alpha}(z,t)X_{O_2}^{\beta}(z,t)M_{N_2O_3} \\ +\frac{k_{oxy}}{K}X_{NO_2}(z,t) - k_{red3}X_{NO}(z,t)X_{red}(z,t)M_{N_2O_3} \\ +k_{red4}X_{NO_2}(z,t)M_{N_2O_3} \end{bmatrix} \quad (1)$$

$$\left.\frac{dX_{NO_2}}{dz}\right|_t = \frac{s\rho_{Ru/Na-Y}}{FM_{N_2O_3}} \begin{bmatrix} -k_{ads}(y_\infty - y(z,t))X_{NO}(z,t)X_{NO_2}(z,t) + k_{des}y(z,t)X_{H_2O}^3 \\ +k_{desred}X_{red}(z,t)X_{H_2O}^3 y(z,t) + k_{oxy}X_{NO}^{\alpha}(z,t)X_{O_2}^{\beta}(z,t)M_{N_2O_3} \\ -\frac{k_{oxy}}{K}X_{NO_2}(z,t) - k_{red4}X_{NO_2}(z,t)M_{N_2O_3} \end{bmatrix} \quad (2)$$

Orders with respect to NO (α) and O_2 mole fractions (β) for Reaction (II) were determined from the adsorption curves obtained using gas mixtures with different NO and O_2 contents. The values were found to be $\alpha = 0.8$ and $\beta = 0.26$, respectively.

$$\frac{dX_{red}}{dt} = -k_{red3}X_{red}X_{NO} - k_{red4}X_{red}X_{NO_2} \quad (3)$$

$$\left.\frac{dy}{dt}\right|_z - k_{ads}(y_\infty - y(z,t))X_{NO}(z,t)X_{NO_2}(z,t) + k_{des}y(z,t)X_{H_2O}^3 + k_{desred}X_{red}X_{H_2O}^3 y(z,t) = 0 \quad (4)$$

The profiles of $X_{NO}(z, t)$, $X_{NO_2}(z, t)$, $X_{red}(z, t)$ and $y(z, t)$ were calculated from the differential equations (1)–(4) which were numerically integrated by the Euler method, with dt increments of 1 s and dz increments of 1.6×10^{-4} m.

The following boundary conditions apply:

$t = 0,\ y(z, 0) = 0$

$z = 0,\ X_{NO} = X_{0,NO};\ X_{NO_2} = X_{0,NO_2},\ X_{0,NO_2}$ is given by a blank experiment.

And for desorption:

$z = 0,\ X_{NO} = 1000$ ppm; $X_{NO_2} = 0$.

The values of $y(z)$ at the beginning of the desorption step are those obtained at the end of the adsorption step. Since it was found that the amount of NO_x stored after catalyst saturation was about the same whatever the temperature, an average of 2.80×10^{-3} $g_{N_2O_3}/g_{cata}$ was taken as y_∞ input value in the model.

k_{ads}, k_{des}, k_{oxy}, k_{desh2}, k_{redh3} and k_{redh4} are the unknown parameters. The determination of these parameters was done at each temperature by data fitting to reach acceptable agreement with the experimental NO/NO_2 curves.

4.6. Fitting of experimental results

In a first step, k_{ads}, k_{des} were fitted. k_{des} was determined using experimental data obtained in the absence of reducing agent in the desorption phase. The theoretical values of $K = k_{oxy}/k_{-oxy}$ (Reaction (II), see Section 4.1) were used as input of the model at different temperatures. Afterwards, the values of k_{oxy} were fitted to obtain a good agreement between the experimental profiles of NO and NO_2 and the calculated values. k_{-oxy} was obtained by dividing k_{oxy}/K. In the next step k_{desh2}, k_{redh3} and k_{redh4} were estimated. The values of the kinetic parameters used in the simulation of the experimental curves are listed in Table 3.

Fig. 2 depicts the influence of temperature on NO_x adsorption for an inlet mole fraction of NO equal to 1100 ppm. A quite good agreement between the experimental and the calculated values was obtained except at the beginning of the storage process where NO_x adsorption was underestimated by the model. However, the ratio of NO_2/NO was well predicted by the model whatever the temperature.

A comparison between the experimental and the calculated values obtained at 285 °C for different inlet mole fractions of NO is given in Fig. 3. Good agreement was obtained except again at the beginning of the storage step. In the adsorption cycle using 260 ppm NO, the model tended to underestimate NO_x adsorption.

The model tended to overestimate the adsorption profiles at the beginning. This disagreement between the calculated and the experimental values could be explained by the pre-equilibrium stage that occurs before the adsorption step. The pre-equilibrium stage describes the movement or the migration of N_2O_3 molecule before its adsorption on a suitable site in the super cage of Na–Y.

Table 4
y_∞ values ($g_{N_2O_3}/g_{cata}$) taken as model input and kinetic constants obtained for Na–Y at different temperatures. k_{ads}, k_{des} are given in s^{-1}.

T (°C)	y_∞	k_{ads}	k_{des}
257	5.4×10^{-3}	107,000	28
267	5.3×10^{-3}	92,000	27
285	5.2×10^{-3}	76,000	25
315	4.8×10^{-3}	48,000	22

Many parameters could affect this pre-equilibrium stage such as geometrical factor of the frame, the right configuration of N_2O_3, availability and suitability of sites for N_2O_3 adsorption that are not taken into account in the model.

An acceptable agreement between the experimental and calculated NO and NO_2 outlet mole fractions was obtained at 268 °C at different concentrations of O_2 (from 2.5% to 15%) as shown in Fig. 4.

The adequacy of the model for describing the NO_x desorption/reduction steps in the presence of different concentrations of reducing agent (H_2) is illustrated in Fig. 5. The model reproduced the peak NO_x release observed experimentally. For 7000 ppm H_2 or 3000 ppm H_2, a good agreement between computed and experimental NO, NO_2 and NO_x concentration profiles was obtained (Fig. 5). NO is partially reduced by 1000 ppm H_2 as shown in Fig. 5. However NO_2 conversion is overestimated in this case.

The model reproduced the experimental observation that hydrogen had a very strong influence on the desorption kinetics, while the water concentration had little influence.

The kinetic parameters determined for Na–Y zeolite without ruthenium, published elsewhere [33] and for Ru/Na–Y obtained in the present work are substantially different (Tables 3 and 4). The values of k_{ads} fitted for Ru/Na–Y are higher than those determined for pure Na-Y. The $k_{ads(Na-Y)}$ values are ranging from 48,000 s^{-1} to 107,000 s^{-1} (Table 4). The $k_{ads(Na-Y)}$ and $k_{ads(Ru/Na-Y)}$ values are of the same order of magnitude. For the desorption phase, the estimated values of $k_{des(Ru/Na-Y)}$ are different form the values of $k_{des(Na-Y)}$. The $k_{des(Na-Y)}$ values are comprised between 22 s^{-1} and 28 s^{-1}.

To verify the sensitivity of the model to the values of the kinetic constants, NO_x adsorption curves were computed using the kinetic parameters (k_{ads}, k_{des}) determined for Na–Y and compared to experimental curves (Fig. 6). The agreement was poor, showing that the adsorption and desorption kinetic parameters determined for co-adsorption of NO and NO_2 on Na–Y zeolite did not permit to obtain a good description for NO_x adsorption on Ru/Na–Y zeolite. The strong differences between fitted kinetic constants for adsorption and desorption of NO_x on Na–Y and Ru/Na–Y suggests that besides the catalytic role assigned to ruthenium it may also somehow have an influence on the adsorption sites of the Na–Y zeolite. Remarkably, on Ru/Na–Y all the kinetic constants except k_{oxy} and k_{-oxy} were temperature independent (Table 3). In contrast to this, the kinetic constants k_{ads} and k_{des} on Na–Y adsorbent without ruthenium decrease significantly with temperature (Table 4).

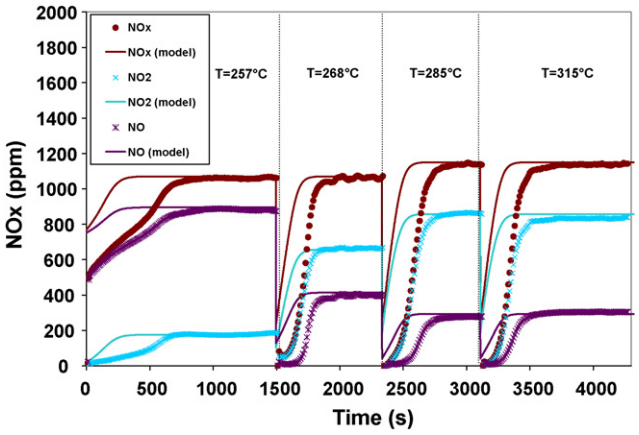

Fig. 6. Experimental NO_x adsorption curves (data points) and model (solid lines) using k_{ads} and k_{des} determined for Na–Y [30] at the outlet of Ru/Na–Y adsorbent bed at different temperatures for an adsorbing gas mixture of 1100 ppm NO, 5% O_2, 12% H_2O and balance helium.

The temperature dependence of the kinetic constant k_{oxy} obeyed Arrhenius law:

$$k_{oxy} = 1.1619 \times 10^{17} \exp\left(\frac{-188,000}{RT}\right)$$

Physico-chemical characterization of the Ru/Na–Y zeolite adsorbent in different states during NO_x adsorption–desorption–reduction as done previously for the Na–Y adsorbent [27] will be needed to trace the origin of the differences in behavior.

The model could be refined by adding a detailed description of the oxidation and reduction of the ruthenium phase. Nevertheless, given the approximations, the model already grasps the main features of this interesting NO_x adsorbent.

5. Conclusions

Ru/Na–Y zeolite can be operated in NO_x adsorption–desorption–reduction cycles involving an alternation of simulated lean burn and rich gas mixture and temperatures of 257–315 °C. NO_x saturation capacities were found to be almost constant in the temperature range of 257–315 °C. Ruthenium dispersed over Na–Y zeolite was highly active in oxidation of NO to NO_2 needed to achieve adsorption on Na–Y zeolite. A one-dimensional fixed-bed model was developed, simulating the experimental outlet NO_x concentrations at different temperatures and gas compositions. In the model, NO is oxidized into NO_2 on ruthenium sites. NO and NO_2 are assumed to be co-adsorbed as N_2O_3 molecules in the network of sodium cations and water molecules in the supercages of Na–Y zeolite. NO_x desorption and reduction in the presence of hydrogen was also simulated. Kinetic constants of nitric oxide oxidation as well as of NO_x adsorption, desorption and reduction by hydrogen were estimated by data fitting. The proposed model showed a reasonable agreement with experimental data. The kinetic constant of NO oxidation showed Arrhenius behavior. The kinetic constants of NO_x adsorption and desorption were temperature independent. The discrepancy of adsorption kinetic constants on Na–Y and Ru/Na–Y suggest that the ruthenium phase besides catalyzing oxidation and reduction reactions also seems to modify the NO_x adsorption sites.

Acknowledgments

The authors gratefully thank Dr. M. Mokhtari and Dr. E. Godard for their help. Financial support of this work has been provided by the European Union (Brite/Euram program AHEDAT) which is gratefully acknowledged by the authors. SH is grateful to FWO Vlaanderen for a research grant. JAM acknowledges the Flemish Government for long-term structural funding (Methusalem). JFB acknowledges REALISE (Réseau Alsace de Laboratoire en Ingénierie et Sciences pour l'Environnement).

References

[1] R. Zhang, A. Villanueva, H. Alamdari, S. Kaliaguine, Appl. Catal. A 307 (2006) 85–97.
[2] H. Tanaka, I. Tan, M. Uenishi, M. Kimura, K. Dohmae, Top. Catal. 16/17 (2001) 1–4.

[3] M. Devadas, O. Kröcher, M. Elsener, A. Wokaun, G. Mitrikas, N. Söger, M. Pfeifer, Y. Demel, L. Mussmann, Catal. Today 119 (2007) 137–144.
[4] B.J. Adelmana, W.M.H. Sachtler, Appl. Catal. B 14 (1997) 1–11.
[5] O. Kröcher, M. Devadas, M. Elsener, A. Wokaun, N. Söger, M. Pfeifer, Y. Demel, L. Mussmann, Appl. Catal. B 66 (2006) 208–216.
[6] L.J. Alemany, L. Lietti, N. Ferlazzo, P. Forzatti, G. Busca, E. Gianello, F. Bergani, J. Catal. 155 (1995) 117–130.
[7] P. Granger, F. Dhainaut, S. Pietrzik, P. Malfoy, A.S. Mamede, L. Leclercq, G. Leclercq, Top. Catal. 39 (2006) 65–76.
[8] S. Matsumoto, Catal. Today 29 (1996) 43–45.
[9] R. Sounak, M.S. Hegde, G. Madras, Appl. Energy 86 (2009) 2283–2297.
[10] H.Y. Huang, R.Q. Long, R.T. Yang, Appl. Catal. B 33 (2001) 127.
[11] S. Hodjati, K. Vaezzadeh, C. Petit, V. Pitchon, A. Kiennemann, Appl. Catal. B 26 (2000) 5.
[12] E. Fridell, M. Skoglundh, B. Westerberg, S. Johansson, G. Smedler, J. Catal. 183 (1999) 196.
[13] H. Arai, M. Machida, Catal. Today 22 (1994) 97.
[14] I. Nova, L. Castoldi, L. Lietti, E. Tronconi, P. Forzatti, F. Prinetto, G. Ghiotti, J. Catal. 222 (2004) 377.
[15] V.R. Gangwal, C.M.L. Scholz, M.H.J.M. de Croon, J.C. Schouten, Chem. Eng. Sci. 62 (2007) 516–5175.
[16] C.M.L. Scholz, K.M. Nauta, M.H.J.M. de Croon, J.C. Schouten, Chem. Eng. Sci. 63 (2008) 2843–2855.
[17] C.-Y. Sung, L.J. Broadbelt, R.Q. Surr, Catal. Today 136 (2008) 64–75.
[18] S. Matsumoto, Catal. Today 90 (2004) 183–190.
[19] P. Engström, A. Amberntsson, M. Skoglundh, E. Fridell, G. Smedler, Appl. Catal. B 22 (1999) L241.
[20] S. Matsumoto, Y. Ikeda, H. Suzuki, M. Ogai, N. Miyoshi, Appl. Catal. B 25 (2000) 115.
[21] H. Mahzoul, L. Limousy, J.F. Brilhac, P. Gilot, J. Anal. Appl. Pyrol. 56 (2000) 179.
[22] S. Hodjati, C. Petit, V. Pitchon, A. Kiennemann, Appl. Catal. B 30 (2001) 247.
[23] W.E. Adisson, R.M. Barrer, J. Chem. Soc. 757 (1955).
[24] A.G. Panov, R.G. Tonkyn, M.L. Balmer, C.H.F. Peden, A. Malkin, J.W. Hoard, SAE Technical Paper 2001-01-3571, 2001, p. 43.
[25] S. Yoon, A.G. Panov, R.G. Tomkyn, A.C. Ebeling, S.E. Barlow, M.L. Balmer, Catal. Today 72 (2002) 251.
[26] O. Monticelli, R. Loenders, P.A. Jacobs, J.A. Martens, Appl. Catal. B 21 (1999) 215.
[27] A. Sultana, R. Loenders, O. Monticelli, C. Kirschhock, P.A. Jacobs, J.A. Martens, Angew. Chem. Int. Ed. 39 (2000) 2934.
[28] K. Villani, C.E.A. Kirschhock, D. Laing, G. Van Tendeloo, J.A. Martens, Angew. Chem. Int. Ed. 45 (2006) 3106–3109.
[29] A. Sultana, D.D. Habermacher, C.E.A. Kirschhock, J.A. Martens, Appl. Catal. B 48 (2004) 65.
[30] W.E. Addison, R.M. Barrer, J. Chem. Soc. (1955) 757–769.
[31] B.J. Adelman, G.D. Lei, W.M.H. Sachtler, Catal. Lett. 28 (1994) 119–130.
[32] E. Ito, Y.J. Mergler, B.E. Nieuwenhuys, H. van Bekkum, C.M. van den Bleek, Micropor. Mater. 4 (1995) 455–465.
[33] J.F. Brilhac, A. Sultana, P. Gilot, J.A. Martens, Environ. Sci. Technol. 36 (2002) 1136.
[34] N. de Nevers, Air Pollution Control Engineering, McGraw-Hill, New York, 1995, p. 394.
[35] A. Amberntsson, E. Fridell, M. Skoglundh, Appl. Catal. B 46 (2003) 429.
[36] H. Ohtsuka, Appl. Catal. B 33 (2001) 325.
[37] S.J. Schmieg, B.K. Cho, S.H. Oh, SAE Technical Paper 2001-01-3565, 2001.
[38] V. Tschamber, M. Jeguirim, K. Villani, J.A. Martens, P. Ehrburger, Appl. Catal. B 72 (2007) 299–303.
[39] M. Shelef, Catal. Rev. Sci. Eng. 11 (1975) 1.
[40] T.P. Kobylinski, B.W. Taylor, J. Catal. 33 (1974) 376.
[41] I. Nova, L. LIetti, L. Castoldi, E. Tronconi, P. Forzatti, J. Catal. 239 (2006) 244.
[42] J. Després, M. Elsener, M. Koebel, O. Kröcher, B. Schnyder, A. Wokaun, Appl. Catal. B 50 (2004) 73–82.
[43] Z. Li, M. Flytzani-Stephanopoulos, J. Catal. 182 (1999) 313.
[44] L. Olsson, B. Westerberg, H. Persson, E. Fridell, M. Skoglundh, B. Andersson, J. Phys. Chem. B 103 (1999) 10433.
[45] J. Abmann, V. Narkhede, L. Khodeir, E. Löffler, O. Hinrichsen, A. Birkner, H. Over, M. Muhler, J. Phys. Chem. B 108 (2004) 14634.
[46] M. Mahzoul, Ph.D. Thesis, Mulhouse, 1999.
[47] A. Hornung, M. Muhler, G. Ertl, Top Catal. 11/12 (2000) 263–270.